Folding at the Microscale: Enabling Multifunctional 3D Origami-Architected Metamaterials

Zhaowen Lin, Larissa S. Novelino, Heming Wei, Nicolas A. Alderete, Glaucio H. Paulino,* Horacio D. Espinosa,* and Sridhar Krishnaswamy*

Mechanical metamaterials inspired by the Japanese art of paper folding have gained considerable attention because of their potential to yield deployable and highly tunable assemblies. The inherent foldability of origami structures enlarges the material design space with remarkable properties such as auxeticity and high deformation recoverability and deployability, the latter being key in applications where spatial constraints are pivotal. This work integrates the results of the design, 3D direct laser writing fabrication, and in situ scanning electron microscopic mechanical characterization of microscale origami metamaterials, based on the multimodal assembly of Miura-Ori tubes. The origami-architected metamaterials, achieved by means of microfabrication, display remarkable mechanical properties: stiffness and Poisson's ratio tunable anisotropy, large degree of shape recoverability, multistability, and even reversible auxeticity whereby the metamaterial switches Poisson's ratio sign during deformation. The findings here reported underscore the scalable and multifunctional nature of origami designs, and pave the way toward harnessing the power of origami engineering at small scales.

1. Introduction

Architected metamaterials, whose global properties are dictated by those of their constituents and their specific geometrical arrangement, exhibit a number of remarkable phenomena including, but not limited to, mechanical anisotropy,[1] high shape recoverability,[2–4] multistability,[5] and high strength-to-density ratios.[6] Despite the rich design space, facilitated by the multitude of manufacturing techniques, the actual fabrication of structures that integrate more than one feature, specifically shape recoverability with pronounced directional mechanical properties, remains elusive. Particularly within the subset of

periodic plate- and shell-based lattice metamaterials, origami architectures have emerged as a promising pathway to augment the accessible design space by enabling highly deployable[7] and tunable structures[8–10] endowed with unusual mechanical properties,[11–15] poised for multifunctional applications. In addition, the inherent foldability of origami patterns circumvents what is arguably the most detrimental feature of plate and shell-based lattices: very limited recoverability owing to premature failure brought on by stress concentrations at member junctions.

While 3D origami structures have been produced at the macroscale through additive manufacturing techniques such as 3D printing with digital light processing[16] and multi-material printing,[17] achieving the folding properties displayed in ideal paper-origami remains a challenge. The latter follows from the inherent stiffness of the thermoset polymers used in 3D printing, which in turn requires the incorporation of artifacts (e.g., flexible hinges) to attain the necessary foldability in macroscale origami structures. In this context, the reduced bending stiffness at the micro- and nanoscale offer a natural platform to realize artifact-free and single-material origami foldability, thus retaining the most remarkable properties of origami designs and highlighting their scalability in both size and property space (e.g., flaw tolerance). However promising, the roadmap to microscale origami engineering is not free of challenges (e.g., material handling, processing, and metrology), an issue that has limited origami demonstrations primarily to individual unit cells (characteristic dimensions of 20 µm[18] and 200 µm[19]) and foldable nanosheets,[20,21] as opposed to more complex 3D functional systems. Here, using a characteristic panel dimension of 13.83 µm, we leverage nanoscale effects and integrate them into an origami design framework to produce the smallest 3D origami-architected metamaterials which successfully retain its most outstanding properties without having to resort to artifacts to enable folding.

The specific origami architecture that is the focus of this work is based on the coupling of Miura-Ori tubes in a zipper/aligned assembly, which exhibits strong anisotropic macroscale response.[22] As shown in **Figure 1**a,b, the individual tubes are assembled from two mirrored Miura-Ori strips, enabling flat-foldability in two directions. The kinematics of the resultant structure is defined by the panel angle α, dimensions

Z. Lin, H. Wei, N. A. Alderete, Dr. H. D. Espinosa, Dr. S. Krishnaswamy
Department of Mechanical Engineering
Northwestern University
Evanston, IL 60208, USA
E-mail: espinosa@northwestern.edu; sridhar.krishnaswamy@northwestern.edu

L. S. Novelino, Dr. G. H. Paulino
Department of Civil and Environmental Engineering
Georgia Institute of Technology
Atlanta, GA 30318, USA
E-mail: paulino@gatech.edu

The ORCID identification number(s) for the author(s) of this article can be found under https://doi.org/10.1002/smll.202002229.

**ADVANCED
SCIENCE NEWS**

www.advancedsciencenews.com

NANO · MICRO

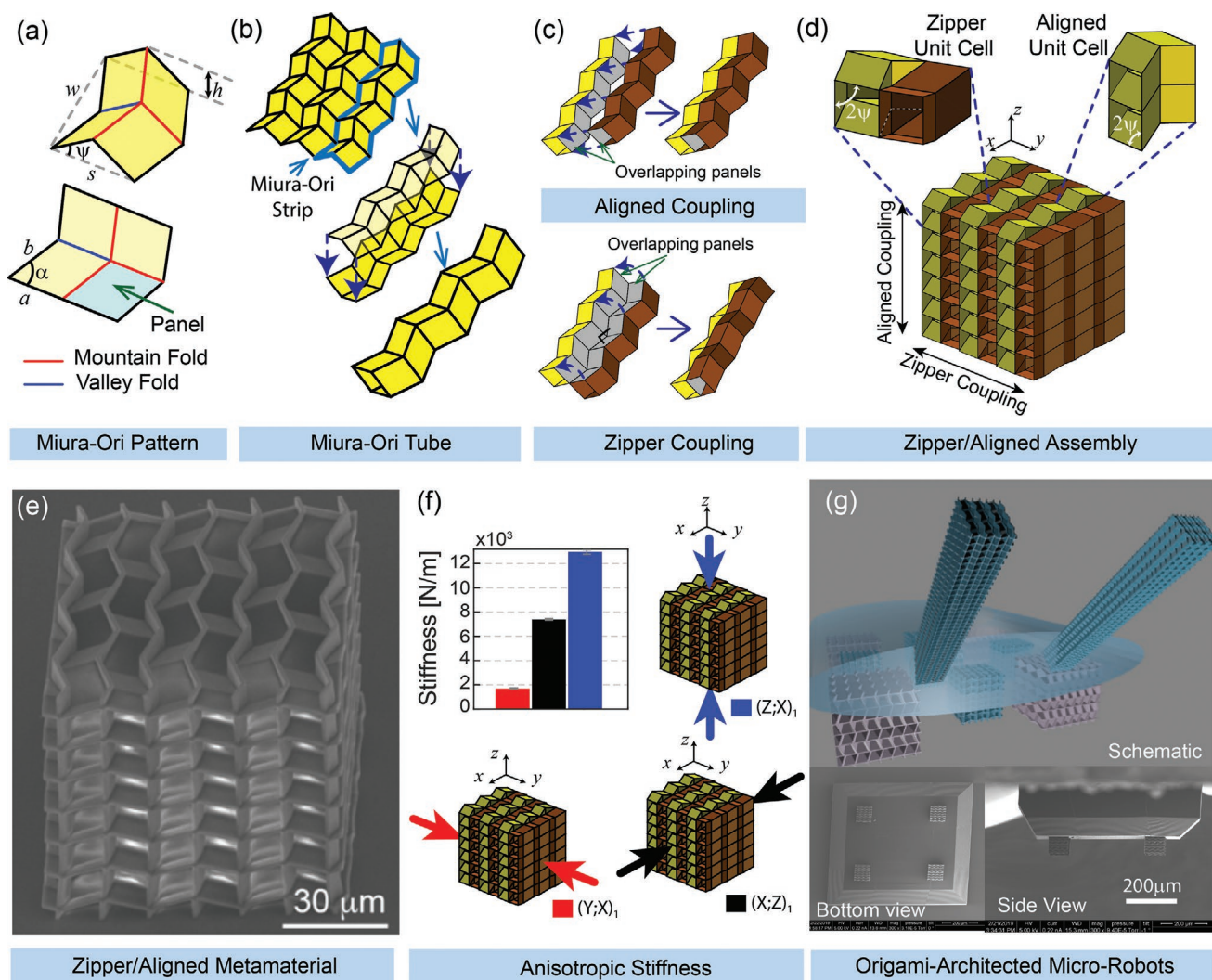**small**

www.small-journal.com

Figure 1. Zipper/aligned metamaterials. a) Partially folded Miura-Ori unit cell and crease pattern. b) Miura-Ori pattern and tube assembly. c) Aligned and zipper coupling of Miura-Ori tubes. d) Schematics and e) SEM image of the zipper/aligned metamaterial. f) Initial axial stiffness of the fabricated Configuration A metamaterial along Cartesian directions. g) Applications to origami-architected microbots: conceptual schematic and SEM images of prototype.

a and b, and are a function of the folding angle ψ. Following single tube assembly, multiple tubes are connected in an aligned and zipper fashion along the Z- and Y-directions, respectively (Figure 1c), and replicated along Cartesian directions. The assembled structure, like the Miura-Ori tube from which it is derived, is deployable in the X- and Y-directions (Figure 1d), but unfoldable in the Z-direction.

To showcase the degree of origami foldability and multifunctionality attained by the proposed framework, we employed two variants of the zipper/aligned assembly with tubes of identical panel lengths $a = b = 13.83 \ \mu m$, angle $\alpha = 75°$, and thickness 1.1 μm, but different initial folding angles ψ_0. The different initial folding angles result in the fabricated structures having distinct natural states (i.e., equilibrium states in absence of external loading) and lead to markedly different structural responses. Configuration A ($\psi_0 = 55°$), corresponding to 92.4% of the total extension of a Miura-Ori

tube, exhibits strong anisotropic mechanical properties, negative Poisson's ratio, and excellent shape recoverability. Along the unfoldable Z-direction, it displays increased stiffness and characteristic buckling and cascading collapse failure modes. On the other hand, Configuration B ($\psi_0 = 40°$), corresponding to 97.4% of the total extension of a Miura-Ori tube, displays strain-dependent Poisson's Ratio and a transition to auxeticity stemming from a folding bifurcation. Our metamaterials were fabricated via 3D direct laser writing (DLW), using two-photon lithography with folds and panels made from the same material and with uniform thickness (Figure 1e). Their structural response was characterized using a micromechanical stage inside a scanning electron microscope (SEM), and the results were analyzed and compared with kinematic models as well as nonlinear finite element analysis (FEA) for stiffness and auxetic response, and Bloch–Floquet FEA for mechanical stability.
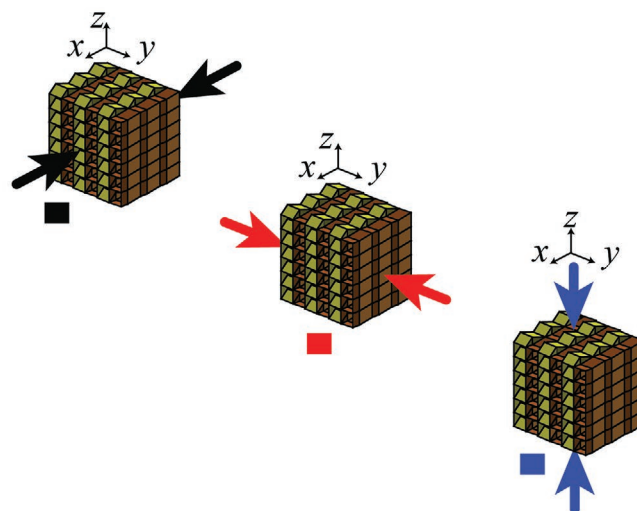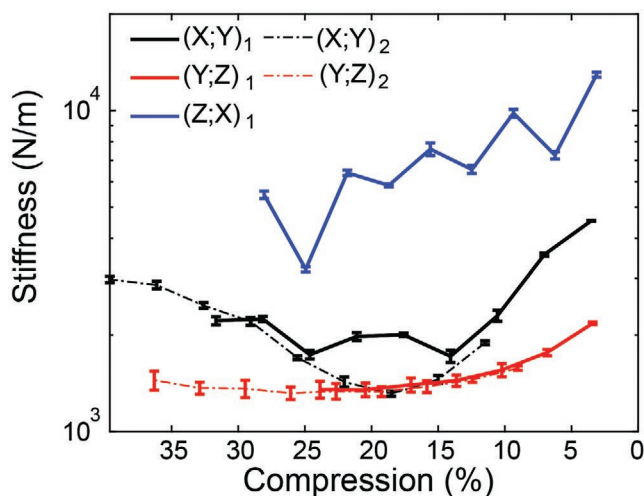
**ADVANCED
SCIENCE NEWS**
www.advancedsciencenews.com

**NANO · MICRO
small**
www.small-journal.com

Figure 2. Anisotropic stiffness. Stiffness as a function of compression in the X-, Y- and Z-directions. The subscripts 1:2 represent first:second compression-release test. The error bars represent one standard deviation. Note that the abscissa (compression percentage) is plotted from right to left, and the ordinate (stiffness) is on a logarithmic scale.

2. Results and Discussion

2.1. Tunable Stiffness Anisotropy Coupled with Shape Recoverability

The aforementioned origami metamaterials exhibit pronounced stiffness anisotropy and stiffness tunability stemming from the fact that the zipper/aligned assembly retains the foldability properties of the Miura-Ori tubes in both X- and Y-directions, but the zipper coupling locks the tubes, preventing the structure from folding when compressed along the Z-direction. The initial stiffness for the Configuration A metamaterial along the Z-direction is almost two times higher than that along the X-direction, and over six times higher than that along the Y-direction, respectively (Figure 1f). The stiffnesses in the foldable X- and Y-directions also decrease with compression by a factor of about two (**Figure 2**). Following viscoelastic recovery, the samples were subjected to a second round of compression-release tests. Accounting for the incomplete viscoelastic recovery, which leads to a more folded residual state, the stiffnesses of the structures upon second compression (denoted by the subscripts "2" in Figure 2) correspond to the initial stiffness at the same level of compression (Section SI, Supporting Information: stiffness response). The latter underscores the importance of the folding angle in the anisotropic stiffness of the metamaterial. Along the Z-direction, the relatively high initial stiffness is due to the unfoldability of the structure along this direction and its decrease, upon compression, is actually a consequence of triggered instabilities as discussed later.

It is also noteworthy that the microscale-enabled foldability in the X- and Y-directions endows the origami assemblies with high shape recoverability in the face of large deformations. Along the Y-direction, after being compressed to a 23% maximum strain, the structure recovers up to 94% (**Figure 3**). Similarly, along the X-direction, after being compressed to 32% average strain, the structure recovers to 93% of its initial height after ≈30 min of relaxation (**Figure 4**). Despite the similar level of recovery, the structures present markedly different stress–strain behaviors in the large deformation regime. Along the Y-direction strain hardening is observed, whereas the X-direction presents a high stress plateau over a long strain regime. The recoverability and resiliency levels observed in these structures, coupled with the post-compression structural integrity, demonstrate their potential for energy absorption applications and highlight their superior performance. This potential could be further harnessed by the expansion of the material space (e.g., use of ceramic coatings).

2.2. Poisson's Ratio Anisotropy and Reversible Auxeticity

Perhaps the most intriguing property of the zipper-coupled origami metamaterials is their ability to exhibit strain dependent Poisson's ratio and reversible auxeticity. This response is predicted using a kinematic model of the zipper/aligned assembly that treats the unit cell defined in **Figure 5**a (see also Section SI, Supporting Information: Auxetic Response) as rigid origami,[23] i.e., composed of rigid panels and perfectly compliant hinges. In this case, the assembly folds rigidly with a single degree of freedom, and the unit cell kinematics can be described by

$$w_x = 2b\sqrt{1 - \frac{\cos^2\alpha}{\cos^2\psi}}, \ \ w_y = 2a\sin 2\psi, \ \ w_z = a, \text{ where } \psi \in [0, \alpha] \quad (1)$$

The Poisson's ratio v_{ij}, defined as the ratio between the strains in the transverse direction j and the loading direction i, is given by

$$v_{xy} = -\frac{\mathrm{d}w_y(\psi)/w_y(\psi)}{\mathrm{d}w_x(\psi)/w_x(\psi)} = \frac{(\cos^2\psi - \cos^2\alpha)(1 - \tan^2\psi)}{\tan^2\psi\cos^2\alpha},$$

$$v_{yx} = \frac{1}{v_{xy}} \text{ and } v_{xz} = -\frac{\mathrm{d}w_z(\psi)/w_z(\psi)}{\mathrm{d}w_x(\psi)/w_x(\psi)} = 0 \quad (2)$$

where $\mathrm{d}w_x(\psi)$ and $\mathrm{d}w_y(\psi)$ refer to the derivatives of panel dimensions w_x and w_y, respectively, with respect to ψ. The

ADVANCED
SCIENCE NEWS
www.advancedsciencenews.com
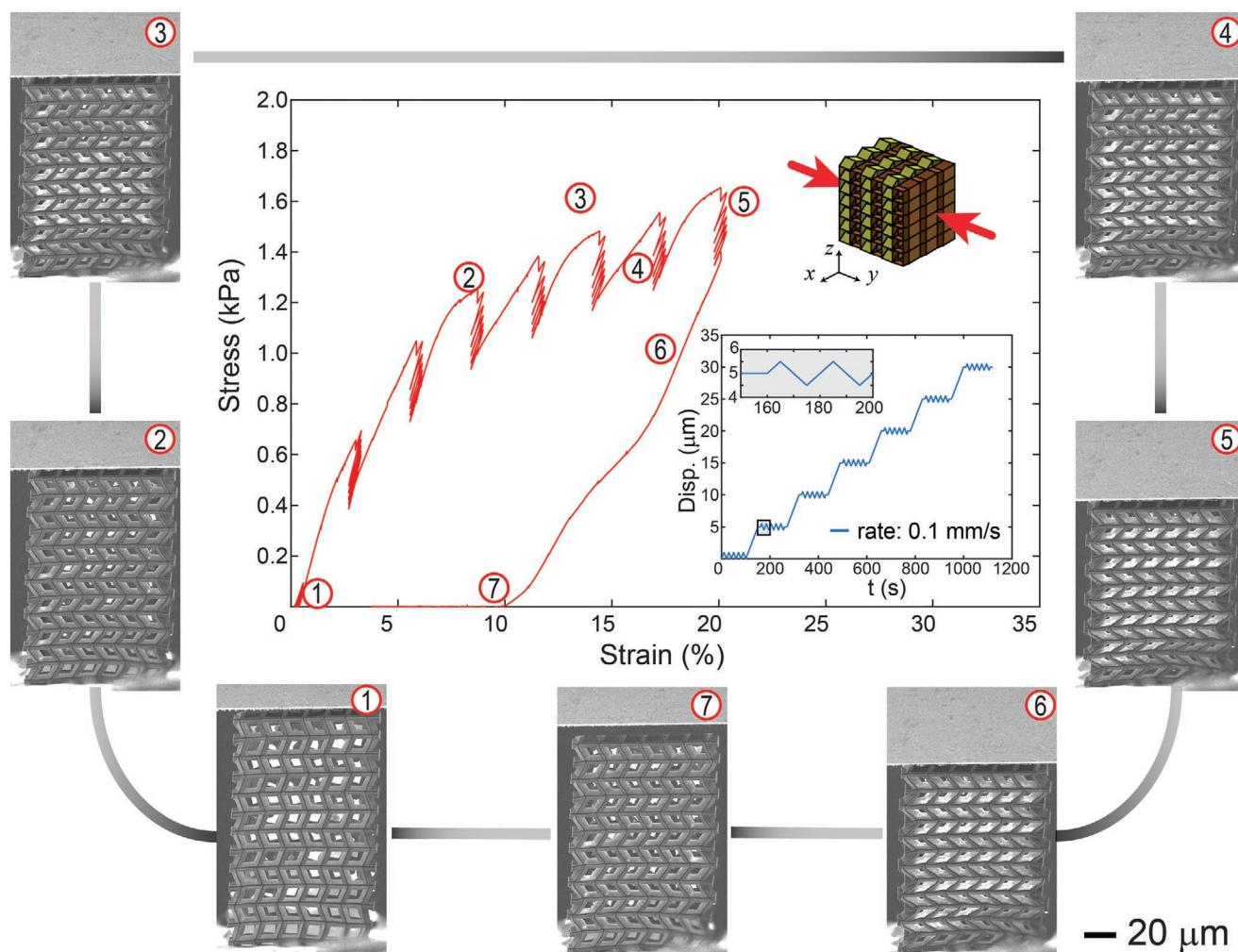
NANO · MICRO
small
www.small-journal.com

Figure 3. Hardening behavior upon compressive loading and recovery of Configuration A along the Y-direction. Outsets 1–4) SEM snapshots of loading phase, outset 5) SEM snapshot of structure at maximum compression, and outsets 6–7) during recovery. Inset shows loading scheme of compression tests.

kinematic model predicts that v_{xz} is always zero independent of the folding angle ψ, while v_{xy} is a function of ψ. In addition, note that if the panel angle $\alpha < 45°$, the zipper/aligned metamaterial will always have $v_{xy} < 0$. However, if $\alpha > 45°$, the Poisson's ratio will change sign depending on the folding angle ψ. While deformation along the X-direction is capable of promoting the full kinematics of the metamaterial (ψ can reach values from 0 to α), deformation along the Y-direction is constrained by the folding angle ψ. At the folding angle $\psi = 45°$, as w_y reaches its maximum, the projections of the panels into the YZ-plane become perpendicular to each other, reaching a critical point in the kinematics of such structures (i.e., further compression along the Y-direction can either lead to a contraction or expansion along the X-direction). This geometric instability produces a Poisson's ratio sign switch when the structure is compressed along the X-direction (Figure 5b,c).

While both Configurations A and B exhibit auxetic behavior (Section SI, Supporting Information: auxetic response), the latter stands out due to its ability to exhibit reversible auxeticity (Figure 5d,e). For samples corresponding to Configuration B, axial and transverse strains measured via image analysis, as the

structure was compressed along the X-direction, are depicted in Figure 5d. It is seen that the transverse strain is initially positive and increases but subsequently decreases and becomes negative upon increasing compression (Figure 5e). This marks a switch in the sign of the Poisson ratio v_{xy} consistent with the kinematic model. Following the gradient definition of the Poisson's ratio,[24] the sign switch occurs at the peak of the transverse strain (point 2 in Figure 5e), which occurs at a critical axial strain of $\varepsilon_{crit} \approx 3.2\%$. Computational simulations (Video S6, Supporting Information), undertaken to provide insight into the mechanisms behind this behavior, show qualitative agreement with experimental results, and confirm that the switch in Poisson's ratio sign stems from a folding bifurcation, evidenced by the peak in the stress–strain response in Figure 5f.

2.3. Instability and Cascading Failure

The intrinsic unfoldability of the origami metamaterials in the Z-direction, a consequence of the zipper assembly configuration, gives rise not only to higher stiffness along this
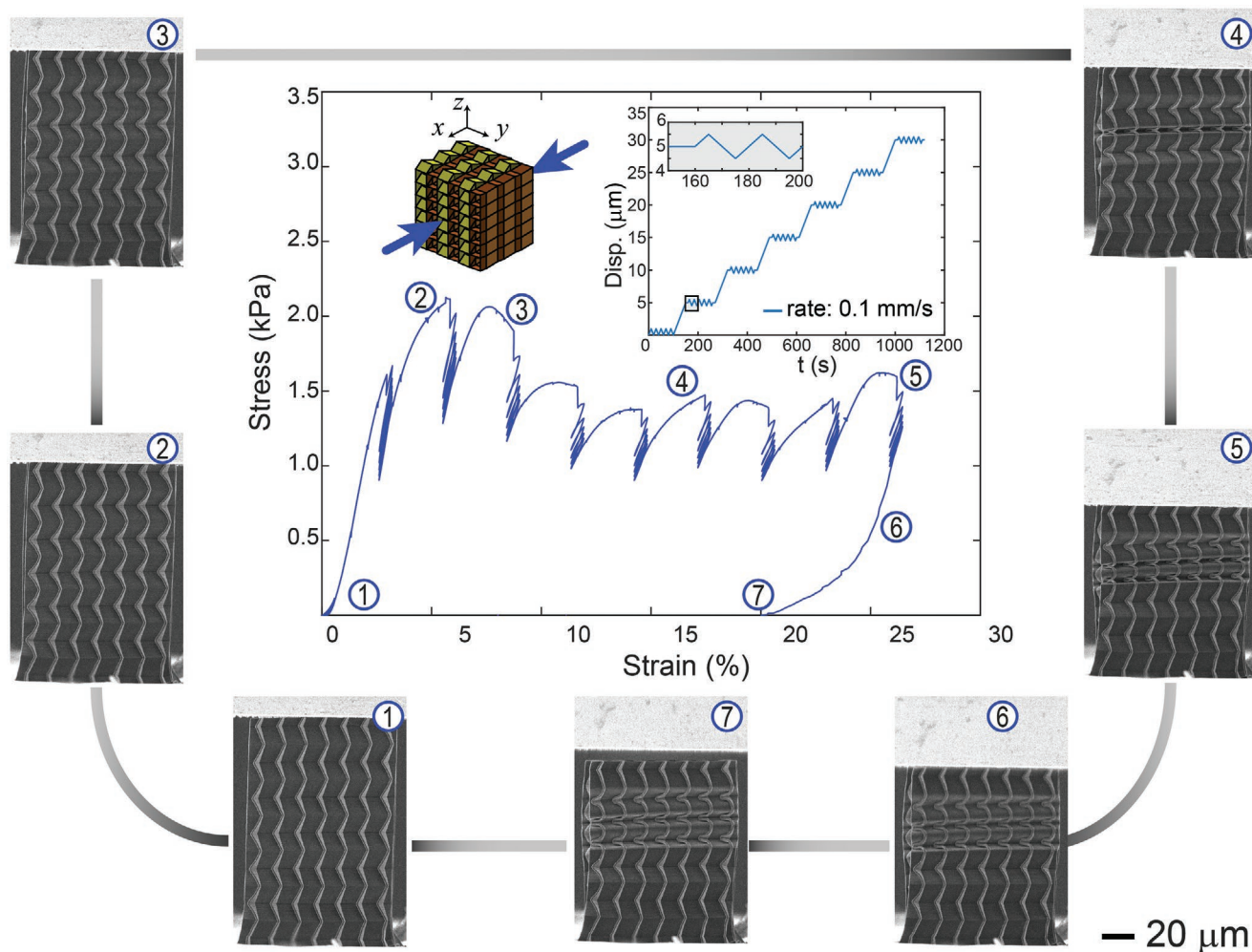
**ADVANCED
SCIENCE NEWS**
www.advancedsciencenews.com

NANO · MICRO
small
www.small-journal.com

Figure 4. Nearly perfectly plastic behavior upon compressive loading and recovery of Configuration A along the *X*-direction. Outsets 1–4) SEM snapshots of loading phase, outset 5) SEM snapshot of the structure at maximum compression, and outsets 6–7) during recovery. Inset shows loading scheme of compression tests.

direction, but also to elastic instability and plastic collapse failure modes. The structure's potential to exhibit elastic instabilities was first investigated by performing elastic finite element simulations on a representative volume element (RVE) subjected to 3D Bloch–Floquet boundary conditions (Section SI, Supporting Information: Modeling—Bloch Analysis and Infinite Periodic Structure). The simulations predicted the existence of an elastic long-wavelength buckling mode, associated with the loss of rank-one convexity of the homogenized elastic moduli tensor. To fully capture the structural response, precluded by the single RVE analysis, geometrically nonlinear finite element analyses of the elastic (E) periodic structure, with increasing number of cells, were performed. The predicted elastic response of the infinite periodic system with the same number of stacked cells as the tested structure, shown in **Figure 6**a, constitutes an upper bound to the structural elastic response and is further discussed in Section SI in the Supporting Information: Modeling—Bloch Analysis and Infinite Periodic Structure. In situ SEM compression experiments along the *Z*-direction of Configuration A samples (Figure 6)

not only confirm the existence of the predicted elastic buckling mode (Figure 6b frames 1–2), but further reveal the finite structure and plasticity effects, evidenced by the occurrence of localization phenomena and cascading plastic collapse failure in a row-wise fashion (Figure 6b, frame 3), (Videos S3 and S7, Supporting Information). To capture such behavior, geometrically nonlinear elastoplastic (EP) finite element analyses of the finite structure (Section SI, Supporting Information: Modeling-FEA) were performed and compared to experimentally obtained results, see Figure 6c. The comparison underscores the prominent role of geometric imperfections in thin-walled structures (Section SI, Supporting Information: Modeling-Imperfection analysis).[25] Local and global imperfections, obtained from a linearized buckling analysis and measurements of fabrication imperfections, were introduced as geometric perturbations to the perfect geometry (see Section SI, Supporting Information: Modeling-Imperfection analysis). The geometric and material nonlinear simulation results show very good agreement with the experimental observations (Figure 6b,c; Video S7, Supporting Information), both in terms

**ADVANCED
SCIENCE NEWS**

www.advancedsciencenews.com
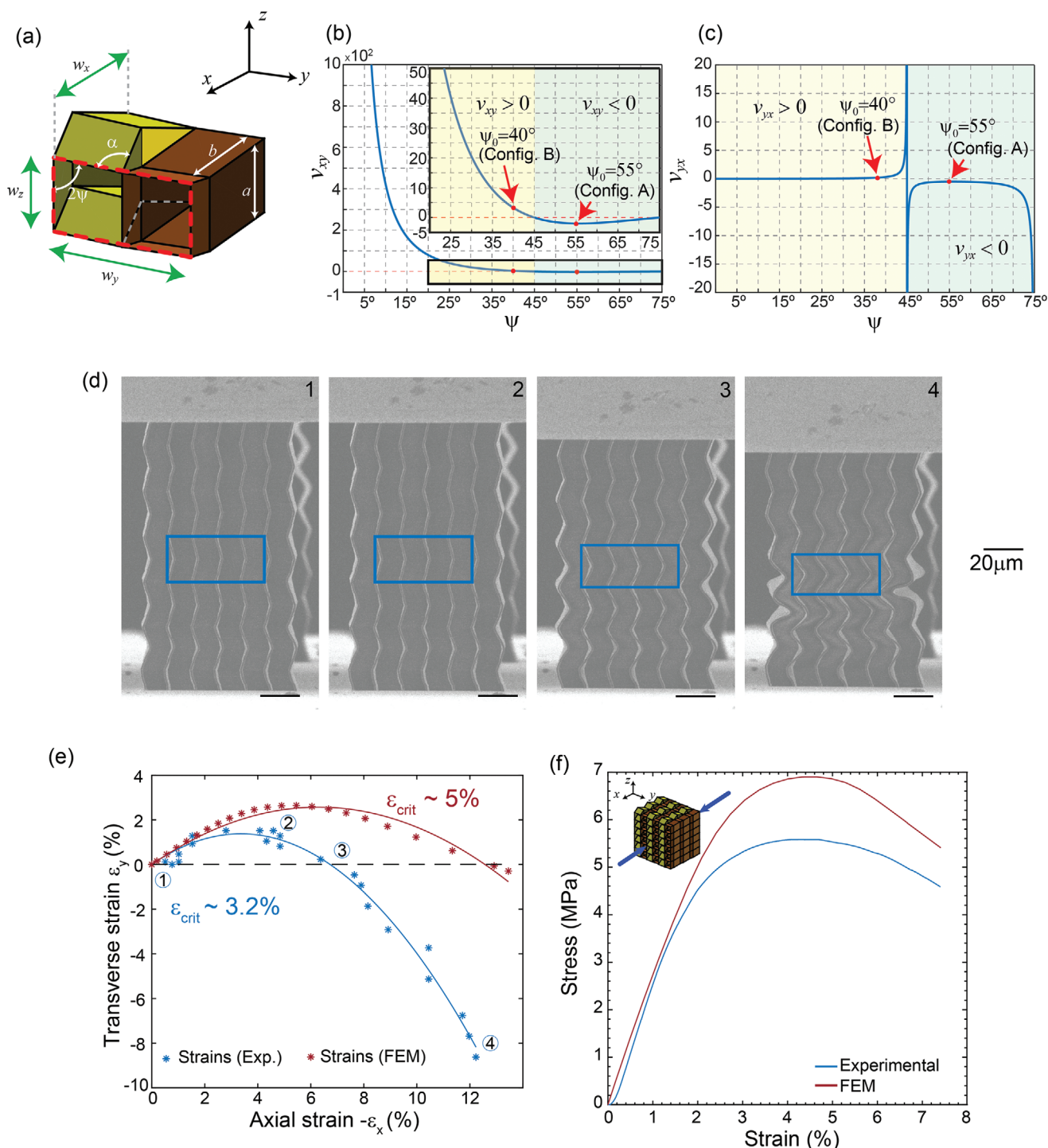
NANO · MICRO

small

www.small-journal.com

Figure 5. Strain dependent Poisson's Ratio and reversible auxeticity. a) Unit cell of the kinematic model of zipper-coupled tubes. b,c) Plots showing Poisson's ratio as a function of the folding angle ψ for panel parameters: $a = b = 13.83$ μm and $\alpha = 75°$. d) SEM snapshots of Configuration B metamaterial at different stages of compression along the X-direction; blue rectangles outline the regions where the Poisson's ratio measurements were made. e) Measured and simulated transverse and axial strains. The numbered points correspond to the images in (d). f) Stress–strain curves from experiments and FEA simulations.

of the structural response of the system (stress–strain curve) and the associated deformation mechanisms (bowing, localization, plastic collapse). Elastoplastic simulations also reveal that while elastic global buckling remains the preferred initial

failure mechanism, localized deformation followed by plastic row collapse ultimately becomes more energetically favorable, leading to the observed post-buckling local failure mechanism (Figure 6b,c). Interestingly, partial recovery of the collapsed
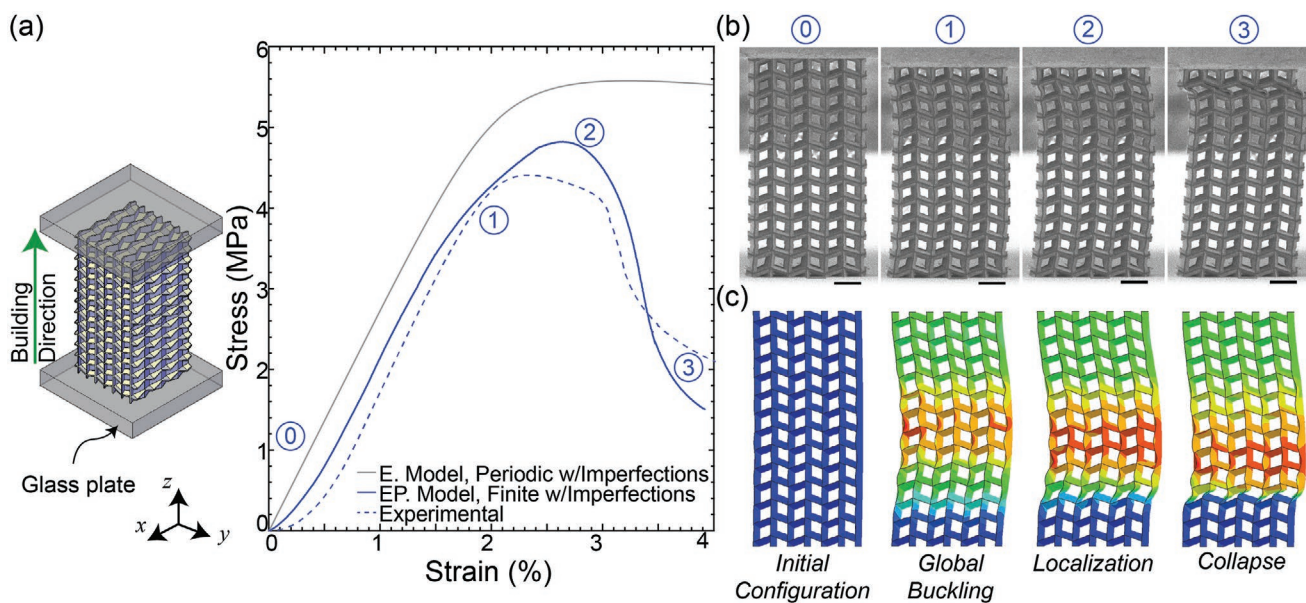
Figure 6. Compression of Configuration A along the unfoldable *Z*-direction. a) Stress–strain curves from experiments, finite-element elastic (E) simulations of infinite periodic structure, and elastoplastic (EP) simulations of the finite size structure with imperfections. b) SEM images depicting the sequence of deformation mechanisms associated to the experimental structural response (scale bar = 20 µm). c) Deformation sequence predicted by the elasto-plastic FEM model of the finite size structure with imperfections.

cells was observed in the experiments upon unloading (Video S7, Supporting Information).

3. Conclusion

Foldability, the core property underlying origami principles, is natural at the micro- and nanoscale due to reduced bending stiffness, as demonstrated in this work. We have exploited the microscale features (e.g., plate thickness) enabled by two-photon direct laser writing to fabricate a variety of 3D origami metamaterials, have measured their mechanical properties using in situ SEM experimentation, and gained mechanistic insight by means of nonlinear computational methods. The structures, based on the coupling of Miura-Ori tubes, constitute the smallest fabricated origami architected metamaterials exhibiting a combination of mechanical properties without precedents. As such, they promise to influence a number of applications across a wide range of fields encompassing the nano-, micro-, and macroscales, leveraging the intrinsic scalability of origami assemblies. In soft microbotics, for example, structural components with highly anisotropic stiffness could be harnessed to carry payloads while maintaining degrees of flexibility for mobility and deployability (Figure 1g). Similarly, the ability to elastically deform in two directions and display elastic instability in a third one could be exploited in complex multimodal actuation and sensing mechanisms. The exhibited anisotropic, deformation-dependent macroscale auxeticity could be harnessed to ingeniously interact with mechanical waves as they relate to wave-guiding, vibrational damping, and energy absorption. The microscale dimension of the developed metamaterials paves the way for applications in the field of medical devices (e.g., deployable stents, microsurgical instruments),

energy harvesting (e.g., auxetic boosters), and other areas where size, shape-morphability and deployability coupled with functionality are requisite attributes.

4. Experimental Section

Fabrication: The origami architected metamaterials were fabricated via 3D DLW, two-photon polymerization technique (Nanoscribe, GmbH), employing a two-photon liquid photoresist (IP-DIP, Nanoscribe). The 3D DLW has a print resolution of 100 nm in plane and 300 nm out-of-plane. The structures were printed on top of a glass slide. To enhance the adhesion between the metamaterial structure and the substrate, the glass slide (fused silica substrate) was cleaned using acetone and isopropyl alcohol (IPA, $p > 99.5\%$), followed by de-ionized (DI) water. A dip-in mode was used wherein a 63× objective lens was immersed into the polymer placed on the substrate where the device was vertically printed in a layer-by-layer fashion.[26] To attain high resolution, a writing speed of 50 µm s^{-1} and a femtosecond laser power of 4 mW were found to be optimal and used for fabricating the metastructures. Subsequent to printing, the structures were developed with propylene-glycol-monomethyl-ether-acetate (PGMEA, $p > 99.5\%$) and rinsed with IPA. Finally, a critical point dryer (Tousimits, SAMDRI-795) was used to dry the structures in a controlled manner to avoid bending.

Two sets of Miura-Ori zipper/aligned architected metamaterials with the same panel lengths $a = b = 13.83$ µm, angle $\alpha = 75°$, and thickness 1.1 µm, but with different initial folding angles ψ_0 were fabricated. The compression direction of the mechanical testing defines the layer-by-layer 3D DLW build direction and dictates the number of unit cells in the printed metamaterial. That is, the number of zipper/aligned unit cells is given by $N_i = 2N$ and $N_j = N_k = N$, where N is typically 3, and the subscript i indicates the build/compression direction, and j, k the perpendicular directions.

Mechanical Testing of Origami Metamaterials: In situ SEM compression tests were performed using a commercial Alemnis nanomechanical test platform (Alemnis AG) set up inside an FEI Nova 600 SEM (Figure S1a, Supporting Information). Both monotonic and oscillatory displacement

profiles were programmed to be exerted by a piezo-driven actuator with a stainless-steel flat punch (1 mm diameter). For the oscillatory scheme (Figure S1b, Supporting Information), applied only to Configuration A, initial loading–unloading cycles were performed with the objective of eliminating any possible hysteresis within the system. Subsequent steps sought to probe the structural elastic response at different levels of compression. Within each load step, the amount of compressive displacement was first increased by 5 µm. Following a holding time of 10 s, the imposed displacement was oscillated with an amplitude of 0.5 µm for five cycles, followed by another 10 s of holding. The unloading portion of the five cycles at each compression level was used for stiffness calculations. In all cases the speed of the flat punch was prescribed to be 0.1 µm s^{-1} and the force was measured by a load cell with a 1 N capacity and 4 µN resolution (root mean square (RMS) noise at 200 Hz).

Configuration A specimens were tested under compression along the three orthogonal directions, labeled as X, Y, and Z in Figure 1d. For each Cartesian direction, two sets of structures were tested and imaged from different orientations (Videos S1–S4, Supporting Information). For instance, the structures compressed in the X-direction were observed from the Y- and Z-directions, denoted as (X;Y) and (X;Z), respectively. After a waiting time to allow for viscoelastic recovery, the structures compressed in the X- or Y-direction were subjected to a second compression test. Numerical subscripts are used to differentiate the results of the first and the second (post recovery) tests on a particular printed structure (e.g., $(X;Y)_1$ and $(X;Y)_2$).

Configuration B specimens were compressed along the X-direction and observed from the Z-direction. As with the samples from Configuration A, two sets of samples were printed and in situ SEM tested (Video S5, Supporting Information).

Micropillar Compression Tests for Material Characterization: Micropillars were fabricated via two-photon polymerization to characterize the constitutive properties of the photocured printing polymer. Printing parameters (i.e., laser power, writing speed) and manufacturing steps were maintained consistent to those in the fabrication of the origami metamaterials. The micropillar tests provided information on the nature of the compressive uniaxial stress–strain behavior of the cured polymer, and served as input for the elastoplastic relations implemented in finite element simulations.

Micropillars were fabricated with a nominal diameter of 8 µm and a length-to-diameter ratio of 3:1 (Figure S2a, Supporting Information). Five replication experiments were performed. Micropillar compression testing was performed using the Alemnis (Alemnis AG) micromechanical test platform under in-situ SEM conditions, using displacement control at a nominal strain rate of $\approx 1 \times 10^{-4}$ s^{-1} with a flat-tip diamond indenter. Applied strains were determined after corrections accounting for thermal drift, machine compliance, micropillar taper, and micropillar-into-substrate sink-in effect.

Yield stresses and strains were estimated using the 0.2% offset rule. Hardening slopes were also computed. Basic statistical analysis was performed to obtain average Young's modulus (E_{avg}), yield stress ($\sigma_{y,avg}$), yield strain ($\varepsilon_{y,avg}$), and Hardening modulus ($E_{p,avg}$). Figure S2b in the Supporting Information presents the stress–strain curves for the micropillar compression experiments described above. Table S1 in the Supporting Information presents the mechanical parameters derived from each test and overall average values with the corresponding sample standard deviations.

Numerical Modeling of Finite Sized Structures: Finite element models of the tested finite-sized structures were implemented in the commercial software ABAQUS to gain qualitative insight into the observed experimental results. Monotonic compression tests of fabricated structures were simulated with pinned boundary conditions at the base. The flat punch compression was simulated by a rigid analytical planar surface in which normal and tangential contact conditions are enforced by a penalty formulation with friction. A friction coefficient $\mu = 0.1$ was employed in the simulations. On account of the computational cost of explicit integrations (i.e., stable time step $\Delta t_c \approx 10^{-10}$ s and experimental time $\Delta t_{exp} > 10^2$ s), implicit integration with nonlinear geometric and material conditions was employed. The employed numerical integration parameters were: maximum number of allowed increments, $N_{increments} = 10^5$, initial time step, $\Delta s_0 = 10^{-4}$, minimum time step, $\Delta s_{min} = 10^{-10}$, and maximum time step, $\Delta s_{max} = 10^{-3}$. The effect of geometric imperfections was accounted for by means of geometric perturbations obtained from a linearized finite element buckling analysis of the perfect geometry. To account for geometric local and global imperfections, a superposition of modes was employed (Section SI, Supporting Information: Modeling-Imperfection analysis). The material properties used in the analysis were obtained from micropillar compression tests (Section SI, Supporting Information: Micropillar Compression Tests for Material Characterization). A bilinear elastic–plastic material law with average Young's modulus ($E = 3097.2$ MPa), hardening modulus ($E_p = 557.8$ MPa) and yield stress ($\sigma_y = 57.8$ MPa) was used in all simulations of finite sized structures. The intrinsic polymer material Poisson ratio was set at $\nu = 0.49$ based on literature data.[3] Following mesh convergence analysis, the average element size was established at $\Delta l \approx 1$ µm using first order triangular and quadrilateral shell elements with reduced integration (Abaqus elements S4R and S3) and five integration points through the thickness.

Bloch–Floquet Numerical Modeling: Leveraging the periodic nature of the Configuration A assembly, the mechanical instability in the unfoldable Z-direction was explored by employing the Bloch–Floquet formalism[27,28] (Section SI, Supporting Information: Bloch Analysis) implemented using the commercial finite element code ABAQUS with appropriate RVE following well-established procedures.[28–31,33] All Bloch simulations were conducted employing first order quadrilateral and triangular shell elements (ABAQUS element types S4R and S3) with five integration points through the thickness. Following mesh convergence studies, the average element size was established at 0.5 µm. The IP-DIP photopolymerized polymer post-cure was modeled as linear elastic with elastic modulus derived from average results from micropillar compression tests (Section SI, Supporting Information: Micropillar compression tests) and reference values for Poisson's ratio ($\nu = 0.49$) and density ($\rho = 1000$ kg m^{-3}).[3,32]

Supporting Information

Supporting Information is available from the Wiley Online Library or from the author.

Acknowledgements

Conflict of Interest

The authors declare no conflict of interest.

Keywords

[1] T. Buckmann, M. Thiel, M. Kadic, R. Schittny, M. Wegener, *Nat. Commun.* **2014**, *5*, 4130.

[2] L. R. Meza, S. Das, J. R. Greer, *Science* **2014**, *345*, 1322.

[3] L. R. Meza, A. J. Zelhofer, N. Clarke, A. J. Mateos, D. M. Kochmann, J. R. Greer, *Proc. Natl. Acad. Sci. USA* **2015**, *112*, 11502.

[4] T. A. Schaedler, A. J. Jacobsen, A. Torrents, A. E. Sorensen, J. Lian, J. R. Greer, L. Valdevit, W. B. Carter, *Science* **2011**, *334*, 962.

[5] S. Waitukaitis, R. Menaut, B. G. G. Chen, M. van Hecke, *Phys. Rev. Lett.* **2015**, *114*, 055503.

[6] J. Bauer, A. Schroer, R. Schwaiger, O. Kraft, *Nat. Mater.* **2016**, *15*, 438.

[7] S. A. Zirbel, B. P. Trease, S. P. Magleby, L. L. Howell, 42nd Aerospace Mechanisms Symp., NASA Goddard Space Flight Center, Greenbelt, MD **2014**, p. 189.

[8] E. Boatti, N. Vasios, K. Bertoldi, *Adv. Mater.* **2017**, *29*, 1700360.

[9] J. L. Silverberg, A. A. Evans, L. McLeod, R. C. Hayward, T. Hull, C. D. Santangelo, I. Cohen, *Science* **2014**, *345*, 647.

[10] Z. J. Wang, L. Q. Jing, K. Yao, Y. H. Yang, B. Zheng, C. M. Soukoulis, H. S. Chen, Y. M. Liu, *Adv. Mater.* **2017**, *29*, 1700412.

[11] K. C. Cheung, T. Tachi, S. Calisch, K. Miura, *Smart Mater. Struct.* **2014**, *23*, 094012.

[12] P. P. Pratapa, K. Liu, G. H. Paulino, *Phys. Rev. Lett.* **2019**, *122*, 155501.

[13] M. Schenk, S. D. Guest, *Proc. Natl. Acad. Sci. USA* **2013**, *110*, 3276.

[14] Z. Y. Wei, Z. V. Guo, L. Dudte, H. Y. Liang, L. Mahadevan, *Phys. Rev. Lett.* **2013**, *110*, 215501.

[15] X. Zhou, S. X. Zang, Z. You, *Proc. R. Soc. A* **2016**, *472*, 20160361.

[16] Z. Zhao, X. Kuang, J. T. Wu, Q. Zhang, G. H. Paulino, H. J. Qi, D. N. Fang, *Soft Matter* **2018**, *14*, 8051.

[17] Q. Ge, C. K. Dunn, H. J. Qi, M. L. Dunn, *Smart Mater. Struct.* **2014**, *23*, 094007.

[18] M. Z. Miskin, K. J. Dorsey, B. Bircan, Y. Han, D. A. Muller, P. L. McEuen, I. Cohen, *Proc. Natl. Acad. Sci. USA* **2018**, *115*, 466.

[19] J. L. Silverberg, J. H. Na, A. A. Evans, B. Liu, T. C. Hull, C. D. Santangelo, R. J. Lang, R. C. Hayward, I. Cohen, *Nat. Mater.* **2015**, *14*, 540.

[20] H. Chen, X. L. Zhang, Y. Y. Zhang, D. F. Wang, D. L. Bao, Y. D. Que, W. D. Xiao, S. X. Du, M. Ouyang, S. T. Pantelides, H. J. Gao, *Science* **2019**, *365*, 1036.

[21] K. J. Si, D. Sikdar, Y. Chen, F. Eftekhari, Z. Q. Xu, Y. Tang, W. Xiong, P. Z. Guo, S. Zhang, Y. R. Lu, Q. L. Bao, W. R. Zhu, M. Premaratne, W. L. Cheng, *ACS Nano* **2014**, *8*, 11086.

[22] E. T. Filipov, T. Tachi, G. H. Paulino, *Proc. Natl. Acad. Sci. USA* **2015**, *112*, 12321.

[23] R. J. Lang, *Twists, Tilings, and Tessellations: Mathematical Methods for Geometric Origami*, CRC Press, Boca Raton, FL **2018**.

[24] G. M. Swallowe, *Mechanical Properties and Testing of Polymers: An A–Z Reference*, Springer, Boston, MA **1999**.

[25] E. Baranger, P. A. Guidault, C. Cluzel, *Compos. Struct.* **2011**, *93*, 2504.

[26] H. M. Wei, S. Krishnaswamy, *Opt. Lett.* **2017**, *42*, 2655.

[27] G. Geymonat, S. Muller, N. Triantafyllidis, *Arch. Ration. Mech. Anal.* **1993**, *122*, 231.

[28] N. Triantafyllidis, B. N. Maker, *J. Appl. Mech.* **1985**, *52*, 794.

[29] M. Aberg, P. Gudmundson, *J. Acoust. Soc. Am.* **1997**, *102*, 2007.

[30] K. Bertoldi, M. C. Boyce, S. Deschanel, S. M. Prange, T. Mullin, *J. Mech. Phys. Solids* **2008**, *56*, 2642.

[31] L. Gong, S. Kyriakides, N. Triantafyllidis, *J. Mech. Phys. Solids* **2005**, *53*, 771.

[32] E. D. Lemma, F. Rizzi, T. Dattoma, B. Spagnolo, L. Sileo, A. Qualtieri, M. De Vittorio, F. Pisanello, *IEEE Trans. Nanotechnol.* **2017**, *16*, 23.

[33] F. Farzbod, M. J. Leamy, *J. Vib. Acoust.* **2011**, *133*, 031010, https://doi.org/10.1115/1.4003202.